Article

Continuous wideband microwave-to-optical converter based on room-temperature Rydberg atoms

Sebastian Borówka [1,2], Uliana Pylypenko[1,2], Mateusz Mazelanik [1,2] & Michał Parniak [1,3] ✉

The coupling of microwave and optical systems presents an immense challenge due to the natural incompatibility of energies, but potential applications range from optical interconnects for quantum computers to next-generation quantum microwave sensors, detectors and coherent imagers. Several of the engineered platforms that have emerged are constrained by specific conditions, such as cryogenic environments, impulse protocols or narrowband fields. Here we employ Rydberg atoms that allow the wideband coupling of optical and microwave photons at room temperature with the use of a modest set-up. We present continuous-wave conversion of a 13.9 GHz field to a near-infrared optical signal using an ensemble of Rydberg atoms via a free-space six-wave mixing process designed to minimize noise interference from any nearby frequencies. The Rydberg photonic converter exhibits a conversion dynamic range of 57 dB and a wide conversion bandwidth of 16 MHz. Using photon counting, we demonstrate the readout of photons of free-space 300 K thermal background radiation at 1.59 nV cm^{-1} rad$^{-1/2}$ s$^{-1/2}$ (3.98 nV cm^{-1} Hz$^{-1/2}$) with a sensitivity down to 3.8 K of noise-equivalent temperature, allowing us to observe Hanbury Brown and Twiss interference of microwave photons.

Coherent conversion between energetically separated domains of microwave (MW) and optical radiation is a demanding issue at the frontier of photonics and quantum science. With the recent progress in the field of quantum computing[1], the most disruptive solution would be a realization of optically connected qubits, which would offer the prospect of hybrid quantum networks[2] and the quantum internet[3]. Several other rapidly developing fields would also greatly benefit from MW–photonic conversion in the near term even with noisy performance, including fundamental[4–6] and observational radioastronomy[7–9], terahertz imaging[10] and next-generation MW sensing[11].

Various approaches to the MW conversion task have been presented using piezo-optomechanics[12–17], electro-optomechanics[18–21],

magneto-optics[22–24], electro-optics[25–30], vacancy centres[31] and Rydberg excitons[32]. Several notable works have realized MW conversion in Rydberg alkali atoms[33–36]. This flexible medium provides a multitude of possible conversion modes with resonant transition frequency scaling as $1/n^3$ for consecutive principal quantum numbers n, and transition dipole moment scaling as n^2, thus allowing excellent sensitivity and subsequent efficiency of conversion. Owing to their MW transitions, Rydberg atoms also have a history of being used in extremely impactful experiments in MW cavity quantum electrodynamics with atomic beams[37–39]. So far all of the works realizing MW-to-optical conversion have required carefully engineered systems, either in the form of developed transducer structures, cryogenic environments or laser-cooled

[1]Centre for Quantum Optical Technologies, Centre of New Technologies, University of Warsaw, Warsaw, Poland. [2]Faculty of Physics, University of Warsaw, Warsaw, Poland. [3]Niels Bohr Institute, University of Copenhagen, Copenhagen, Denmark. ✉e-mail: m.parniak@cent.uw.edu.pl

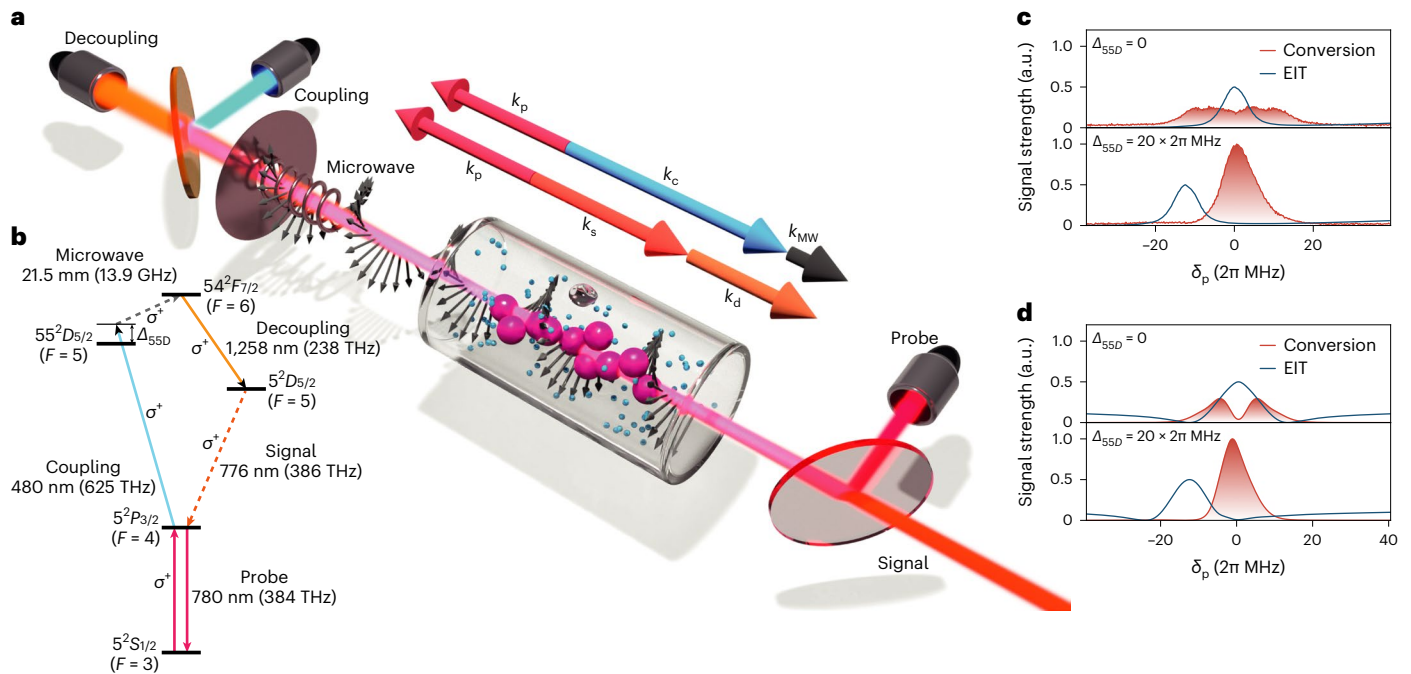**Fig. 1 | Room-temperature MW-to-optical converter. a**, Illustration of a warm vapour Rydberg converter: a circularly polarized MW field enters a rubidium vapour cell, where Rydberg-state atoms, excited in an interaction region defined by three laser beams, contribute to the conversion process and generate a signal beam. The arrows represent the wavevectors k of the interacting fields obeying phase-matching principles. A constant supply of ground-state atoms is ensured by the Maxwellian distribution of velocities, resulting in a continuous process without the need for atomic trapping or repumping. **b**, ^{85}Rb energy-level structure employed in the conversion process. Three strong fields (probe, coupling and decoupling) are applied to the atomic medium in the near-resonant scheme. Introducing the MW field (13.9 GHz) results in a converted emission (signal) at the 776 nm transition. Optimal transduction is ensured with sign-matched σ transitions (between the states of maximal F and m_F quantum numbers). **c**, Comparison of measured EIT and conversion in the domain of probe field detuning (δ_p) for resonant and $55^2D_{5/2}$ level-detuned cases. a.u., arbitrary units. **d**, The same EIT and conversion relation predicted by the numerical simulation. **c,d**, Red shading signifies the total conversion signal photon rate with relation to its zero background.

atoms. The optical interconnection of remote qubits will necessitate a system offering uncompromising performance, but many applications could benefit from noisy converters available in the near term. In this case, it is of particular benefit to employ a simple system, preferably operating at room temperature. Recent works have shown that many quantum devices can be based on hot atomic vapours, including quantum memories[40,41], single-photon sources[42,43] and photonic isolators[44]. With astronomical MW measurements in mind, it is also worth remembering that atomic vapours already play an invaluable role in satellite navigation as a part of atomic clocks[45].

Here we employ a hot-atom system for the task of MW-to-optical upconversion. We demonstrate as a proof of concept that the Doppler-broadened rubidium energy-level structure is well suited to producing atomic coherence resulting in an MW-to-optical converted field. Furthermore, we take advantage of the straightforward nature of the hot-atom approach to present a continuous-wave realization of free-space MW field conversion, in contrast to previous approaches[33–35] in cold atomic media, which had to operate in the impulse regime due to magneto-optical trap operational sequences. Despite the simplicity, we achieve an excellent MW conversion dynamic range, descending down to the thermal limit, where we are able to measure the autocorrelation function of free-space MW thermal photons. The conversion bandwidth is on par with the best results obtained with other wideband conversion media[14,17,24,27,29]. We present the means to tune the conversion band beyond this, and we discuss methods to extend the dynamic range and surpass the thermal limit.

Our idea is based on extending the robust two-photon Rydberg excitation scheme in rubidium, utilized in the measurement of Autler–Townes splitting of electromagnetically induced transparency (EIT) in MW field electrometry[46,47] and atomic receivers[48–50]. We introduce an additional near-infrared (at the higher limit of telecom O-band) laser field, transferring atomic population from a Rydberg state and enabling emission at the $5^2D_{5/2} \rightarrow 5^2P_{3/2}$ (776 nm) transition. This scheme allows robust conversion—free from both noise interference and strong classical fields spectrally close to the signal field. This realization is all-optical and no ancillary MW field is necessary, further simplifying the set-up, as well as broadening its potential applications. We also avoid using ultraviolet fields (employed in the recent work of Kumar et al.[36]), which are particularly problematic both in terms of the generation of narrow-band continuous-wave laser beams and in their destructive impact on optical elements and thus the lifespan of the device.

Results

Conversion in warm Rydberg vapours

Room-temperature atoms in vapour cells are easy to harness experimentally, yet they provide limited options for full quantum control due to Doppler broadening and collisions, which may influence Rydberg atoms in particular. We therefore start by showing that the room-temperature atomic vapours are adequate to facilitate the Rydberg-assisted conversion process. In our demonstration, a cylindrical vapour cell served as a hot-atom Rydberg converter (Fig. 1a; see Methods and Extended Data Fig. 1 for the full set-up of the converter). Three focused optical fields determined an interaction region, where ground-state atoms were supplied from the remainder of the cell via thermal atomic motion, assuring that neither depletion nor other long-term time-dependence occurred, thus enabling a continuous-wave operational framework. These fields combined with a MW field realized coherent (for the measurements of coherence see Supplementary Section 4) six-wave mixing (Fig. 1c) with emission at 776 nm. We utilized sign-matched σ transitions with the largest dipole moments (maximal total angular momentum F and
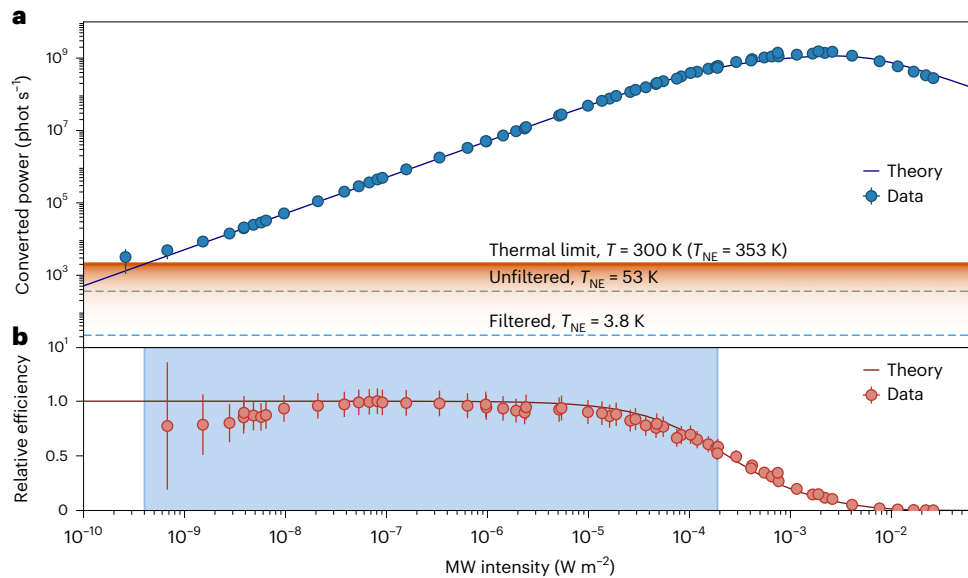
Fig. 2 | MW-to-optical conversion with 57 dB dynamic range. a, Conversion response to the applied MW field intensity from the thermal noise level (2.1×10^3 phot s^{-1}, including thermal radiation and added non-thermal noise, orange solid line) to the conversion saturation limit (1.5×10^9 phot s^{-1}) and the orange shading signifies the parameter region limited by thermal radiation. The observed non-thermal added noise is at the level of a noise-equivalent temperature $T_{NE} = 53$ K (gray dashed line) and can be further filtered down to $T_{NE} = 3.8$ K (blue dashed line). **b**, Relative conversion efficiency (thermal noise subtracted) with a signal-to-noise ratio >1 and relative efficiency >0.5 achieved over a 57 dB dynamic range of the MW intensity from 4.0×10^{-10} to 1.9×10^{-4} W m^{-2} (blue shaded region). The efficiency is normalized to the highest measured value. In both panels we compare the results with a theoretical curve, where the overall efficiency is the only free parameter. The saturation intensity is well reproduced, along with the shape of the curve. The error bars in **a** and **b** are calculated from the photon-counting standard deviation, $\sqrt{\bar{n}}$ (with thermal radiation treated as added noise), where in each case $\bar{n}$ is explicitly noted as photon-counting rates on the y axis, and from the propagation of the calibration's standard deviation.

its projection m_F quantum numbers) driven by circularly polarized fields. The conversion scheme constituted a closed cycle without the need for repumping. The conservation of energy and momentum, governing the wave mixing process, ensured that the temporal and spatial properties of the converted photons were preserved. In contrast to previously presented conversion schemes[33–35], this scheme did not require additional MW fields, and all of the introduced optical fields were sufficiently spectrally different to be separated with the use of free-space optics, even in a collinear configuration.

Considering field detunings from the energy-level structure, we observed that, similarly to ref. 35, the best conversion efficiency was achieved for off-resonant realization, as shown in Fig. 1d in relation to the EIT effect. Here the detuning applied to the Doppler-broadened level structure, involving a range of atomic velocity classes. We found that the detuning from level $55^2D_{5/2}$ played an important role in increasing the efficiency of the conversion, yielding a nearly fivefold improvement in efficiency at detuning $\Delta_{55D} = 20 \times 2\pi$ MHz in comparison with the resonant case.

Continuous-wave conversion

Atomic conversion processes arise from atomic coherences, which in quantum mechanical approaches can be derived from state density matrices $\hat{\rho}$. With the incident weak MW field E_{MW} and strong driving fields we obtained an optical steady-state coherence ρ_s and thus expected emission of the signal field to be $E_s \sim \rho_s = \text{Tr}(|5^2D_{5/2}\rangle\langle5^2P_{3/2}|\hat{\rho}) \sim E_{MW}$. The time evolution of the atomic state is governed by the Gorini–Kossakowski–Sudarshan–Lindblad equation:

$$\partial_t\hat{\rho} = \frac{1}{i\hbar}[\hat{H},\hat{\rho}] + \mathcal{L}[\hat{\rho}], \qquad (1)$$

where ∂_t is derivative over time, $\hat{H}$ is the Hamiltonian and $\mathcal{L}[\cdot]$ is a super-operator responsible for spontaneous emission and other sources of decoherence. In our approach for conversion, we considered the density matrix to be in a steady state, $\partial_t\hat{\rho}(t) = 0$, similarly to EIT-based Rydberg electrometry systems. We employed the steady-state solution of the Gorini–Kossakowski–Sudarshan–Lindblad equation as the basis for the parametric numerical simulation used as an aid to interpret the experimental results we present. We considered a range of atomic velocity classes contributing to the conversion process and took into account the shape of the interaction volume. We found that the conversion was facilitated by ρ_s. Remarkably, ρ_s arises partially due to decoherence and the influx of ground-state atoms into the interaction region.

Our approach can be compared with the pulsed approach to conversion, which requires tailoring of the Hamiltonian $\hat{H}(t)$ (for example by sequentially turning on the driving fields and enabling the conversion for a short time only) to maximize the coherence, and in consequence the conversion output. This approach, showcased particularly in ref. 35, can be implemented in Doppler-free cold-atom systems and leads to high local conversion efficiency, albeit for limited operation times as short as 1/1,000 of a 10 ms time sequence. The potential applications are thus narrowed down to those where the converter can be triggered by a short signal or the aim is to convert a strong classical field. Our continuous-wave approach addresses this gap, enabling uniform, trigger-free conversion of weak or asynchronous signals.

Dynamic range and efficiency

Using a single-photon counter, we measured the converter's response to MW field intensity. As shown in Fig. 2a, the converted signal ranges from 2.1×10^3 to 1.5×10^9 photons per second (phot s^{-1}). We identified the upper bound as saturation from energy-level shifts due to Autler–Townes splitting, and the lower limit as free-space thermal MW photons coupling to the converter. We adjusted for other sources of noise and directional and polarization coupling to the converter (see Extended Data Fig. 2 for directional characteristics) and the measured conversion band. The electric field spectral density level of the observed thermal
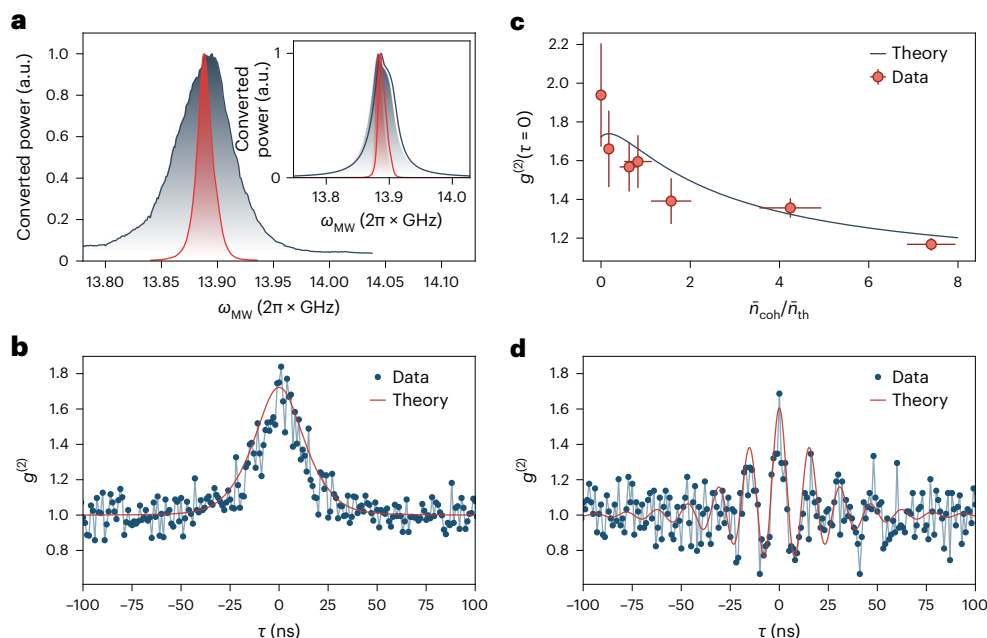
Fig. 3 | Wideband conversion of MW thermal radiation at the single-photon level. a, The dependence of the conversion on MW field detuning (red curve) reveals a bandwidth of $\Gamma_{con} = 16 \times 2\pi$ MHz FWHM. The interdependence of the detunings on the MW and decoupling fields shows that with commensurate detuning of the decoupling field the tunable bandwidth of conversion (dark curve) can be broadened to $59 \times 2\pi$ MHz FWHM. This is in agreement with the general theoretical prediction from the numerical simulation (inset). **b**, Photon autocorrelation (homodyne) measurements yield the second-order autocorrelation function $g^{(2)}$ of the thermal MW photons, confirming the

conversion of quantum thermal state. This experimental result agrees perfectly with parameter-free theory prediction based on the conversion band and measured noise properties. **c**, $g^{(2)}(0)$ decreases with the introduction of coherent state photon rate $\bar{n}_{coh}$, in agreement with the theory. The error bars presented are calculated from $\sqrt{\bar{n}}$ and the propagation of the calibration's standard deviation in relation to the thermal level. **d**, Introducing a far-detuned ($\Delta\omega = 4\Gamma_{con} = 64 \times 2\pi$ MHz) coherent MW field with rate $\bar{n}_{coh} \approx \bar{n}_{th}$ induces interference in the autocorrelation function, with a beat modulation frequency equal to the detuning.

radiation, 1.59 nV cm^{-1} rad$^{-1/2}$ s$^{-1/2}$ (isotropic, both polarizations), agreed very well with the theoretical prediction of 1.64 nV cm^{-1} rad$^{-1/2}$ s$^{-1/2}$ (see the Methods for the derivation). We note, however, that such a remarkable agreement occurred for the model that was simpler than the reality of the experiment; that is, the presence of the MW antenna near the converter was not accounted for. Nevertheless, we were able to confirm the matching of two fundamental references for the MW field intensity, namely the thermal bath and the Autler–Townes splitting.

We determined the efficiency of the implemented conversion: Fig. 2b shows a relative conversion efficiency of >0.5 and a signal-to-noise ratio of >1 (in relation to thermal noise) for 57 dB of MW intensities (from 4.0×10^{-10} to 1.9×10^{-4} W m^{-2}), which we identified as the converter's dynamic range. The data are presented as normalized to the highest measured value. The converter's response to the MW field and conversion efficiency were well predicted by the numerical simulation, where only the overall efficiency was parametrically matched.

As far as the absolute efficiency is concerned, several teams adopted an approach where the reference MW photon rate is taken from the intensity multiplied by the area of the interaction medium[33–35]. Care must be taken when interpreting this area-normalized efficiency, as the interaction region is substantially subwavelength for the MW fields. By adopting the same approach, we obtained a $3.1 \pm 0.4\%$ atomic efficiency (see Supplementary Section 1 for the estimation). We were also able to use our full model to give a theoretical prediction (assuming no signal depletion) for the area-normalized efficiency of $2.8 \pm 1.6\%$ (see Supplementary Section 1 for calculation), which matched the observed value. We expect that for our case, as well as previous free-space experiments, this efficiency would be achieved if the MW mode was confined to the interaction volume, for example by means of a waveguide. For port-coupled or cavity-based conversion[36] the absolute efficiency can be estimated unambiguously.

Conversion band

Using a single-photon counter we measured the conversion's dependence on the MW frequency in the linear response regime (Fig. 3a), arriving at a bandwidth $\Gamma_{con} = 16 \times 2\pi$ MHz full-width at half-maximum (FWHM). Further explorations revealed interdependences on the MW and decoupling (1,258 nm) field detunings that could be utilized as a means of fine-tuning the converter to incoming MW fields. We show that with such a procedure we were able to widen the tunable conversion bandwidth up to $59 \times 2\pi$ MHz FWHM.

Photonic conversion of thermal radiation

We performed single-photon autocorrelation measurements (Fig. 3b) of the thermal radiation signal, confirming the Hanbury Brown and Twiss effect of thermal photon bunching ($g^{(2)}(0) > 1$) for MW photons. The results obtained experimentally agreed perfectly with the parameter-free theory drawn from the Wiener–Khinchin theorem:

$$g^{(1)}_{th}(\tau) = \frac{1}{2\pi} \int_{-\infty}^{\infty} |S(\omega)|^2 e^{-i\omega\tau} d\omega, \qquad (2)$$

where $g^{(1)}$ is first order autocorrelation function (in this case of thermal signal), τ is time delay, $|S(\omega)|^2$ is the normalized ($\int_{-\infty}^{\infty} |S(\omega)|^2 d\omega = 2\pi$) power spectral density, shown in Fig. 3a, measured under the assumption that the thermal radiation has white noise characteristics locally, and ω is angular frequency of signal. Following naturally from this, $g^{(2)}_{th}(\tau) = 1 + |g^{(1)}_{th}(\tau)|^2$. To arrive at the theoretical results presented in Fig. 3b, we considered both the thermal radiation and non-thermal noise present in the system (see Methods for details). An alternative parametric fitting of the exponent function, $g^{(2)}(\tau) = 1 + (g^{(2)}(0) - 1)e^{-2\tau/\tau_0}$, yields $g^{(2)}(0) = 1.868 \pm 0.035$ and a coherence time $\tau_0 = 26.0 \pm 1.5$ ns.
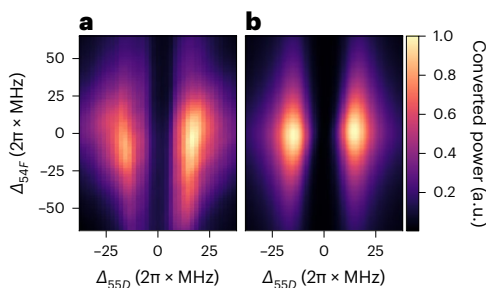
Fig. 4 | Atomic bright resonances enabling the conversion process.
a, Measured conversion in the domain of bare-state detunings from energy levels $55^2D_{5/2}$ and $54^2F_{7/2}$ (other detunings being near zero), revealing the underlying bright resonances $|B+\rangle$ and $|B-\rangle$. From this measurement we obtained the optimal level detunings $\Delta_{55D} = 16 \times 2\pi$ MHz, $\Delta_{54F} = 0$. **b**, The same conversion interdependence predicted by the numerical simulation.

Next we introduced a resonant coherent MW field of comparable strength to the thermal field in terms of the converted photon rates $\bar{n}_{coh}$ for coherent photons and $\bar{n}_{th}$ for thermal photons. We estimated $g^{(2)}(0)$ for consecutive measurements (Fig. 3c) in agreement with the theory. Interestingly, the introduction of a stronger but $\Delta\omega$ far-detuned coherent field, while keeping $\bar{n}_{coh} \approx \bar{n}_{th}$, led to a beat modulation of the autocorrelation function (Fig. 3d). Specifically, in this case:

$$g^{(2)}(\tau) = 1 + \frac{1}{4}\left(\left|g_{th}^{(1)}(\tau) + e^{-i\omega\tau}\right|^2 - 1\right), \qquad (3)$$

where $g_{th}^{(1)}(\tau) = A(\tau)e^{-i\omega_0\tau}$, $A(\tau)$ is a real function (being the result of equation (2)) and ω_0 is the mean frequency of the conversion band. The beat modulation is at the frequency of the detuning $\Delta\omega = \omega - \omega_0$.

Noise figures
With no external field applied to the converter, we observed photons that, by disabling each field and cross-correlation analysis, we identified as consisting of 85% thermal radiation, 13% fluorescence of optical elements induced by the 480 nm laser field and 2% other noise. This proportion resulted in an overall 5.7:1 signal-to-noise ratio; as the signal is thermal in this case, we could translate this straightforwardly to a noise-equivalent temperature $T_{NE} = 53$ K. As the added noise is wide-band, we utilized additional cavity-assisted filtering of the thermal signal, improving the ratio to 77:1, thus $T_{NE} = 3.8$ K. We present these values in Fig. 2a as a reference to the converter's response characteristics. See Supplementary Section 2 for a cross-correlation analysis and comparison of different sources of noise.

Observation of bright resonances
Following the short demonstration of the level-detuned working regime (shown in Fig. 1d), we explored the dependence of the conversion on the detunings from bare atomic levels—realized with proportional detunings of the fields. We found this domain to be the most convenient to operate in, as it naturally obeys the conservation of energy in six-wave mixing. In general, with a hot-atom system, the Doppler effect prevents interpretations as simple as in the cold-atom case. However, in our case, we found that the Doppler effect was mostly cancelled by the selection of velocity classes in the two-photon process: that is, with probe and coupling fields. We expect that the conversion loop was composed of two dressed-state subsystems: the three-level system dressed by the coupling and probe fields, and the two-level system dressed by the decoupling field. By scanning the Δ_{55D} level detuning, we observed resonances corresponding to two bright states: the simplified and unnormalized eigenstates given by
$|B\pm\rangle = \Omega_p^* |5^2S_{1/2}\rangle \pm \sqrt{|\Omega_p|^2 + |\Omega_c|^2}\,|5^2P_{3/2}\rangle + \Omega_c\,|55^2D_{5/2}\rangle$ (* denotes

complex conjugation) split by roughly Ω_c (as seen in Fig. 4), where Ω_p and Ω_c are the Rabi frequencies of the probe and coupling fields, respectively. The dark state $|D\rangle = \Omega_c^* |5^2S_{1/2}\rangle - \Omega_p |55^2D_{5/2}\rangle$ does not take part in the conversion process, but could be accessed in a cavity-enhanced system to yield conversion with lower loss due to $5P_{3/2}$ state decay. On the other hand, as we swept the detuning Δ_{54F}, we observed broadening, rather than clear splitting into two dressed states $|\pm\rangle = |54^2F_{7/2}\rangle \pm |5^2D_{5/2}\rangle$, which was due to interference of different velocity classes. Using numerical studies, we found that this splitting was observed only at much higher decoupling Rabi frequencies in different scans. We also note that the blue-detuned resonance resulted in a slightly stronger conversion than the red-detuned resonance, which we attribute to the interfering effect of other energy levels (that may take part in the wave-mixing process) on the latter. Our observations confirm that bright resonances $|B\pm\rangle$ are essential in the conversion process. The conversion process was optimized by accessing one of the resonances through detuning from the two-photon resonance (and thus also avoiding the dark resonance $|D\rangle$), as seen in Fig. 1c and observed in other free-space experiments[35].

Discussion
The proof-of-concept warm-atomic converter presented here exhibits flexibility in terms of a high dynamic range and wide bandwidth, which supports its potential for applications. We anticipate that the fields of contemporary astronomy could benefit from conversion-based MW photonic measurements[4–9], where Rydberg atoms excel in simplicity, adaptability and presented low noise figures. As the conversion scheme utilized here is all-optical, it can be applied in similar systems (that is, cold trapped atoms and superheterodyne Rydberg electrometry) to avoid the introduction of noise by spectrally close fields. We highlight many desirable properties of the converter. The ability to perform photon counting of MW radiation at room temperature, along with observations of Hanbury Brown and Twiss interference and coherent–thermal interference, is important, as these typically require deeply cryogenic conditions[51]. The converter presents an extremely large dynamic range and excellent bandwidth, along with many options for both fine and very coarse tuning to different Rydberg levels. The all-optical realization offers further prospects for applications as even strong electromagnetic interference would not damage the device. This could be important for MW-based communication, where another advantage may come from avoiding shot noise of homodyne detection via photon counting.

There are numerous issues that are outside the scope of this work and could be explored in more detail to increase the range and efficiency of the conversion. As thermal photons are spread over the whole conversion band, the limit approached in Fig. 2a is not fundamental—efficient narrow spectral filtering or phase-locking measurements could push it downwards, enabling detection at the single-photon level. The non-thermal noise may be decreased further, for example by utilizing different optical elements in the set-up (specifically addressing the 480 nm fluorescence) or by exploring noncollinear configurations of the laser fields. Various optimization efforts could also be performed to find working points with greater conversion efficiency, although the operational regime of warm atomic vapours and strong probe fields does not allow for simple theoretical predictions. The converter's response to MW pulses is yet to be investigated, as are pulse-control of laser fields or coherent repumping of atomic population, although the complexity of the set-up would then inevitably increase. The operation mode of the Rydberg converter could in principle also be shifted to adapt to emission at the telecom C-band wavelength—specifically, the $4^2D_{5/2}$ to $5^2P_{3/2}$ transition occurs at 1,530 nm.

All-optical operation could be retained when designing a set-up that exploits the cancellation of the Doppler effect at a wider scope (that is, using different transitions), enabling more atoms to take part in the conversion process. Conversely, a range of atomic velocities

may offer the means to further widen the tunable conversion band. We believe that with commensurate detunings of all-optical field, the tunable conversion bandwidth could be extended to as much as 600 MHz (the width of Doppler-broadened probe absorption line); if the neighbouring Rydberg transitions are considered, the converter could efficiently cover the full range of MW frequencies up to 50 GHz solely by tuning the laser fields. Such an ultrawide adaptable conversion band would only be possible with warm Rydberg atomic vapours. Finally, we also expect that the reverse process of optical-to-MW conversion should be facilitated by our set-up via coupling of atoms to MW resonators (see Supplementary Section 6 for details).

We anticipate that further progress will be centred around introducing warm Rydberg atomic vapours to MW cavity systems, as this would enhance the coupling between the MW field and atomic interaction volume. Our all-optical scheme is well suited to that task; in comparison, six-wave mixing schemes involving two MW transitions would require a doubly resonant cavity with close, but non-degenerate, resonances. The design principles for hot-atom MW-cavity systems can be drawn from cavity-enhanced atomic clocks. Even with moderate finesse, we expect the conversion efficiency to be substantially enhanced, probably even leading to radiative cooling of the cavity mode via conversion. At the same time, considerable potential lies in recent progress in the microfabrication of atomic devices[52], such as micro- and nanoscale vapour cells[53,54] and hollow-core photonic bandgap fibres filled with alkali atoms[55]. These instruments may enable all-fibre reproducible applications of our converter's model, paving the way to next-generation MW-converting sensors.

Online content

Any methods, additional references, Nature Portfolio reporting summaries, source data, extended data, supplementary information, acknowledgements, peer review information; details of author contributions and competing interests; and statements of data and code availability are available at https://doi.org/10.1038/s41566-023-01295-w.

References

1. Arute, F. et al. Quantum supremacy using a programmable superconducting processor. *Nature* **574**, 505–510 (2019).
2. Muralidharan, S. et al. Optimal architectures for long distance quantum communication. *Sci. Rep.* **6**, 20463 (2016).
3. Awschalom, D. et al. Development of quantum interconnects (QuICs) for next-generation information technologies. *PRX Quantum* **2**, 017002 (2021).
4. Riechers, D. A. et al. Microwave background temperature at a redshift of 6.34 from H_2O absorption. *Nature* **602**, 58–62 (2022).
5. Pankratov, A. L. et al. Towards a microwave single-photon counter for searching axions. *npj Quantum Inf.* **8**, 61 (2022).
6. Komatsu, E. New physics from the polarized light of the cosmic microwave background. *Nat. Rev. Phys.* **4**, 452–469 (2022).
7. Greaves, J. S. et al. Anomalous microwave emission from spinning nanodiamonds around stars. *Nat. Astron.* **2**, 662–667 (2018).
8. Gorski, M. D. et al. Discovery of methanimine (CH_2NH) megamasers toward compact obscured galaxy nuclei. *Astron. Astrophys.* **654**, A110 (2021).
9. Kou, Y. et al. Microwave imaging of quasi-periodic pulsations at flare current sheet. *Nat. Commun.* **13**, 7680 (2022).
10. Wade, C. G. et al. Real-time near-field terahertz imaging with atomic optical fluorescence. *Nat. Photon.* **11**, 40–43 (2016).
11. Xia, Y. et al. Demonstration of a reconfigurable entangled radio-frequency photonic sensor network. *Phys. Rev. Lett.* **124**, 150502 (2020).
12. Bochmann, J., Vainsencher, A., Awschalom, D. D. & Cleland, A. N. Nanomechanical coupling between microwave and optical photons. *Nat. Phys.* **9**, 712–716 (2013).
13. Forsch, M. et al. Microwave-to-optics conversion using a mechanical oscillator in its quantum ground state. *Nat. Phys.* **16**, 69–74 (2019).
14. Jiang, W. et al. Efficient bidirectional piezo-optomechanical transduction between microwave and optical frequency. *Nat. Commun.* **11**, 1166 (2020).
15. Mirhosseini, M., Sipahigil, A., Kalaee, M. & Painter, O. Superconducting qubit to optical photon transduction. *Nature* **588**, 599–603 (2020).
16. Hönl, S. et al. Microwave-to-optical conversion with a gallium phosphide photonic crystal cavity. *Nat. Commun.* **13**, 2065 (2022).
17. Stockill, R. et al. Ultra-low-noise microwave to optics conversion in gallium phosphide. *Nat. Commun.* **13**, 6583 (2022).
18. Andrews, R. W. et al. Bidirectional and efficient conversion between microwave and optical light. *Nat. Phys.* **10**, 321–326 (2014).
19. Peairs, G. et al. Continuous and time-domain coherent signal conversion between optical and microwave frequencies. *Phys. Rev. Appl.* **14**, 061001 (2020).
20. Arnold, G. et al. Converting microwave and telecom photons with a silicon photonic nanomechanical interface. *Nat. Commun.* **11**, 4460 (2020).
21. Delaney, R. D. et al. Superconducting-qubit readout via low-backaction electro-optic transduction. *Nature* **606**, 489–493 (2022).
22. Hisatomi, R. et al. Bidirectional conversion between microwave and light via ferromagnetic magnons. *Phys. Rev. B* **93**, 174427 (2016).
23. Bartholomew, J. G. et al. On-chip coherent microwave-to-optical transduction mediated by ytterbium in YVO_4. *Nat. Commun.* **11**, 3266 (2020).
24. Zhu, N. et al. Waveguide cavity optomagnonics for microwave-to-optics conversion. *Optica* **7**, 1291–1297 (2020).
25. Rueda, A. et al. Efficient microwave to optical photon conversion: an electro-optical realization. *Optica* **3**, 597–604 (2016).
26. Witmer, J. D. et al. A silicon-organic hybrid platform for quantum microwave-to-optical transduction. *Quantum Sci. Technol.* **5**, 034004 (2020).
27. McKenna, T. P. et al. Cryogenic microwave-to-optical conversion using a triply resonant lithium-niobate-on-sapphire transducer. *Optica* **7**, 1737–1745 (2020).
28. Xu, Y. et al. Bidirectional interconversion of microwave and light with thin-film lithium niobate. *Nat. Commun.* **12**, 4453 (2021).
29. Sahu, R. et al. Quantum-enabled operation of a microwave-optical interface. *Nat. Commun.* **13**, 1276 (2022).
30. Wang, C. et al. High-efficiency microwave-optical quantum transduction based on a cavity electro-optic superconducting system with long coherence time. *npj Quantum Inf.* **8**, 149 (2022).
31. Lekavicius, I., Golter, D. A., Oo, T. & Wang, H. Transfer of phase information between microwave and optical fields via an electron spin. *Phys. Rev. Lett.* **119**, 063601 (2017).
32. Gallagher, L. A. P. et al. Microwave-optical coupling via Rydberg excitons in cuprous oxide. *Phys. Rev. Res.* **4**, 013031 (2022).
33. Han, J. et al. Coherent microwave-to-optical conversion via six-wave mixing in Rydberg atoms. *Phys. Rev. Lett.* **120**, 093201 (2018).
34. Vogt, T. et al. Efficient microwave-to-optical conversion using Rydberg atoms. *Phys. Rev. A* **99**, 023832 (2019).
35. Tu, H.-T. et al. High-efficiency coherent microwave-to-optics conversion via off-resonant scattering. *Nat. Photon.* **16**, 291–296 (2022).
36. Kumar, A. et al. Quantum-enabled millimetre wave to optical transduction using neutral atoms. *Nature* **615**, 614–619 (2023).
37. Goy, P., Fabre, C., Gross, M. & Haroche, S. High-resolution two-photon millimetre spectroscopy in sodium Rydberg states: possible applications to metrology. *J. Phys. B* **13**, L83–L91 (1980).

38. Raimond, J. M., Goy, P., Gross, M., Fabre, C. & Haroche, S. Collective absorption of blackbody radiation by Rydberg atoms in a cavity: an experiment on Bose statistics and Brownian motion. *Phys. Rev. Lett.* **49**, 117–120 (1982).

39. Meschede, D., Walther, H. & Müller, G. One-atom maser. *Phys. Rev. Lett.* **54**, 551–554 (1985).

40. Finkelstein, R., Poem, E., Michel, O., Lahad, O. & Firstenberg, O. Fast, noise-free memory for photon synchronization at room temperature. *Sci. Adv.* **4**, eaap8598 (2018).

41. Kaczmarek, K. T. et al. High-speed noise-free optical quantum memory. *Phys. Rev. A* **97**, 042316 (2018).

42. Ripka, F., Kübler, H., Löw, R. & Pfau, T. A room-temperature single-photon source based on strongly interacting Rydberg atoms. *Science* **362**, 446–449 (2018).

43. Dideriksen, K. B., Schmieg, R., Zugenmaier, M. & Polzik, E. S. Room-temperature single-photon source with near-millisecond built-in memory. *Nat. Commun.* **12**, 3699 (2021).

44. Dong, M.-X. et al. All-optical reversible single-photon isolation at room temperature. *Sci. Adv.* **7**, eabe8924 (2021).

45. Steigenberger, P. et al. Galileo orbit and clock quality of the IGS multi-GNSS experiment. *Adv. Space Res.* **55**, 269–281 (2015).

46. Sedlacek, J. A. et al. Microwave electrometry with Rydberg atoms in a vapour cell using bright atomic resonances. *Nat. Phys.* **8**, 819–824 (2012).

47. Jing, M. et al. Atomic superheterodyne receiver based on microwave-dressed Rydberg spectroscopy. *Nat. Phys.* **16**, 911–915 (2020).

48. Deb, A. B. & Kjærgaard, N. Radio-over-fiber using an optical antenna based on Rydberg states of atoms. *Appl. Phys. Lett.* **112**, 211106 (2018).

49. Meyer, D. H., Cox, K. C., Fatemi, F. K. & Kunz, P. D. Digital communication with Rydberg atoms and amplitude-modulated microwave fields. *Appl. Phys. Lett.* **112**, 211108 (2018).

50. Borówka, S., Pylypenko, U., Mazelanik, M. & Parniak, M. Sensitivity of a Rydberg-atom receiver to frequency and amplitude modulation of microwaves. *Appl. Opt.* **61**, 8806 (2022).

51. Chen, Y.-F. et al. Microwave photon counter based on Josephson junctions. *Phys. Rev. Lett.* **107**, 217401 (2011).

52. Kitching, J. Chip-scale atomic devices. *Appl. Phys. Rev.* **5**, 031302 (2018).

53. Cutler, T. et al. Nanostructured alkali-metal vapor cells. *Phys. Rev. Appl.* **14**, 034054 (2020).

54. Lucivero, V. G., Zanoni, A., Corrielli, G., Osellame, R. & Mitchell, M. W. Laser-written vapor cells for chip-scale atomic sensing and spectroscopy. *Opt. Express* **30**, 27149 (2022).

55. Peters, T., Wang, T.-P., Neumann, A., Simeonov, L. S. & Halfmann, T. Single-photon-level narrowband memory in a hollow-core photonic bandgap fiber. *Opt. Express* **28**, 5340 (2020).

Methods

Density matrix calculation

As indicated in the main text, we solved the five-level Gorini–Kossakowski–Sudarshan–Lindblad equation in the steady state (that is $\partial_t \hat{\rho} = 0$). The Lindbladian was constructed from the Hamiltonian and the jump operators using the QuantumOptics.jl package[56]. We next solved for the steady state using standard linear algebra methods, finding the zero eigenvalue. We employed jump operators $\hat{J}_n$ for spontaneous decay and for transit-time decay; that is, atoms exiting the interaction region with ground-state atoms entering. Each solution was for a given set of Rabi frequencies, detuning and a specific velocity class v (along the longitudinal direction). The detunings were modified due to the Doppler effect as $\Delta_n^v = \Delta_n \pm k_n v$ with $n \in \{p, c, MW, d\}$. We next averaged the resulting state-state density matrix $\hat{\rho}$ over the Doppler velocity profile with weighting function $f(v) = \sqrt{m/2\pi k_B T} \exp(-mv^2/k_B T)$ (where m is the ^{85}Rb atomic mass and k_B the Boltzmann constant) and over the Gaussian profile of the beams due to changing Rabi frequencies. Unless noted otherwise, the MW Rabi frequency was taken well below the saturation point. Finally, we extracted the generated signal, always plotted as intensity, as $|E_s|^2 \sim |\mathrm{Tr}\,(|5^2D_{5/2}\rangle \langle 5^2P_{3/2}|\hat{\rho})|^2$ or the EIT signal as $\mathrm{Im}\,(\mathrm{Tr}\,(|5^2S_{1/2}\rangle \langle 5^2P_{3/2}|\hat{\rho}))$.

Phase matching

Efficient conversion requires all atoms interacting with the MW field to emit in phase. This renders the phase-matching condition that determines the conversion efficiency depending on the MW field mode. Thus we introduced the phase-matching factor $\eta_{phm}(\theta)$ for a plane wave MW field $E_{MW}(\theta)$ entering the medium at angle θ to the propagation axis (z). The factor was then calculated by projecting the generated electric susceptibility onto the detection mode u_s, a Gaussian beam focused in the centre of the cell ($z_0 = 0$) with $w_0 = 100\,\mu m$. To obtain the projection we assumed the spatial dependence of the susceptibility to be in the form of the product of all interacting fields. This is a simplification compared with the full model, as in general the steady-state density matrix and, in turn, the coherence ρ_s, have a more complex dependence on strong drive field amplitudes. Nevertheless, for the purpose of spatial calculations, the simplified approach yields correct results and the susceptibility then takes on the form:

$$\chi_\theta = E_p E_p^* E_c E_d^* E_{MW}(\theta), \qquad (4)$$

with the optical fields (E_p, E_c, E_d) taken to be Gaussian beams with the same z_0 and w_0 as the detection mode u_s. We also accounted for the relatively strong absorption of the probe field (E_p) by multiplying its amplitude by the exponential decay $\exp(-\alpha z)$ with (measured) $\alpha = 19\,m^{-1}$. Finally, the coefficient was calculated as the following integral:

$$\eta_{phm}(\theta) = \int_{-L/2}^{L/2} dz \int_0^{2\pi} d\phi \int_0^\infty \rho\, d\rho \chi_\theta u_s^*, \qquad (5)$$

where $L = 50\,mm$ is the length of the glass cell.

Thermal modes. We next estimated the effective field root-mean-square amplitude due to thermal blackbody radiation in our conversion band, which takes our converter being both polarization and wavevector sensitive into account. To do so, we followed a standard derivation of Planck's law; however, when considering all electromagnetic modes, we accounted for both the polarization dependence and phase matching during conversion. The effective mean-square field amplitude at temperature T can be written as follows:

$$\langle E_{eff}^2 \rangle = \frac{\omega^2 \langle \mathcal{E} \rangle}{\pi^2 c^3 \varepsilon_0} \frac{1}{4\pi} \int_0^{2\pi} d\phi \int_0^\pi d\theta \sin(\theta)|\eta(\theta)|^2, \qquad (6)$$

$$\langle \mathcal{E} \rangle = \frac{\hbar \omega}{e^{\hbar\omega/k_B T} - 1}, \qquad (7)$$

where ω is the frequency of the MW field, c is the speed of light and ε_0 is vacuum permittivity. Importantly, $\eta(\theta)$ is the field conversion efficiency coefficient that arises from projecting the MW field in the plane-wave modes at a given angle θ onto circular polarization along the conversion axis and multiplying it by the phase-matching factor:

$$|\eta(\theta)|^2 = \left(\cos\left(\frac{\theta}{2}\right)^4 + \sin\left(\frac{\theta}{2}\right)^4 \right) |\eta_{phm}(\theta)|^2. \qquad (8)$$

In fact, the efficiency $|\eta(\theta)|^2$ represents the converter reception pattern, which we plot in the Extended Data Fig. 2. From the pattern we saw that the contribution to the effective noise-equivalent field at temperature T comes mostly from the phase-matched MW coming from an almost right-angled cone with the correct circular polarization. Finally, we referred the effective field convertible by the atoms $\sqrt{\langle E_{eff}^2 \rangle}$ to total root-mean-square field fluctuations $\sqrt{\langle E^2 \rangle}$, which can be calculated by plugging in $|\eta(\theta)|^2 = 2$ (because of two polarizations).

In Fig. 2a we show that the thermal radiation level (without added non-thermal noise) corresponds to $3.41 \times 10^{-10}\,W\,m^{-2}$ or $5.07\,\mu V\,cm^{-1}$, as calibrated from the Autler–Townes splitting at large fields. To calculate the spectral field density, we considered the conversion bandwidth using an integral measure $\bar{\Gamma}_{con} = 1/\max(|S(\omega)|^2) \int_{-\infty}^\infty |S(\omega)|^2 d\omega = 17.8 \times 2\pi\,MHz$ to arrive at $\sqrt{\langle E_{eff}^2 \rangle} = 480\,pV\,cm^{-1}\,(rad/s)^{-1/2}$. This is highly consistent with the model prediction of $\sqrt{\langle E_{eff}^2 \rangle} = 495\,pV\,cm^{-1}\,(rad/s)^{-1/2}$. When referred to the total field fluctuations, we obtained the results presented in the main text, that is $\sqrt{\langle E^2 \rangle} = 1.59\,nV\,cm^{-1}\,(rad/s)^{-1/2}$ (measured) and $\sqrt{\langle E^2 \rangle} = 1.64\,nV\,cm^{-1}\,(rad/s)^{-1/2}$ (predicted) (for a detailed analysis of photon rates and electric field densities see Supplementary Section 3).

Thermal and coherent state autocorrelation function

We considered the autocorrelation measurements with three different sources of photons, defined by rates: $\bar{n}_{th}$ for thermal state photons, $\bar{n}_{coh}$ for coherent state photons and $\bar{n}_{noise}$ for photons coming from wide-band, non-interfering sources (for example, various forms of fluorescence). We follow the derivation presented in ref. 57 (and later showcased in refs. 13,36) to arrive at the following general form of second-order autocorrelation function:

$$g^{(2)}(\tau) = 1 + \frac{\left| \bar{n}_{th} g_{th}^{(1)}(\tau) + \bar{n}_{coh} e^{-i\omega\tau} \right|^2 - \bar{n}_{coh}^2}{\left(\bar{n}_{th} + \bar{n}_{coh} + \bar{n}_{noise} \right)^2}, \qquad (9)$$

where ω is the coherent state frequency. In Fig. 3b,c,d $\bar{n}_{noise}/\bar{n}_{th} = 15/85$, in Fig. 3d $\bar{n}_{coh}/\bar{n}_{th} = 100/85$.

The $g_{th}^{(1)}$ correlation function was obtained from the power spectral density in Fig. 3a via the Wiener–Khinchin theorem (equation (2)), and then used to calculate $g^{(2)}$ for comparison with the experiment. The conversion bandwidth was measured via photon-counting detection in the domain of the MW field detuning: we directly changed the MW frequency fed to the antenna. The next crucial step to equate the measured conversion bandwidth with the power spectral density of thermal radiation coupling to the converter $|S(\omega)|^2$ was to assume that the thermal radiation had white noise characteristics within our band of interest (that is, for free uncoupled radiation $|S(\omega)|^2 = \mathrm{const}$). We then arrived at the function presented in Fig. 3b.

Laser field parameters

The laser beams were focused to equal Gaussian waists of $w_0 = 100\,\mu m$ and combined with the use of dichroic mirrors (Extended Data Fig. 1f). The probe beam counterpropagated with respect to the other fields

and its transmission through the ^{85}Rb medium was then utilized as a means of calibration via EIT effects (Fig. 1d,e). The length of the vapour cell was 50 mm. The collinear laser field configuration was facilitated with $4f$ optical systems (not shown on the scheme) with mirrors at focal planes, enabling independent control of every beam's position and propagation angle. The effective peak Rabi frequencies used for the 780 nm, 480 nm and 1258 nm laser fields were derived from the numerical simulation as $\Omega_p = 8 \times 2\pi$ MHz, $\Omega_c = 22 \times 2\pi$ MHz and $\Omega_d = 17 \times 2\pi$ MHz respectively. The optimal dominant detuning from the $55D$ level was measured as $\Delta_{55D} = 16 \times 2\pi$ MHz (Fig. 4a) and was used for the other measurements, with the other detunings being near zero. For Fig. 1 and Extended Data Fig. 1e the MW Rabi frequency was set to about $\Omega_{MW} = 8 \times 2\pi$ MHz, while for the Figs. 3 and 4a it was deep inside the unsaturated regime. For the Fig. 4a the decoupling intensity was increased to about $\Omega_d = 25 \times 2\pi$ MHz peak. The calibration of detuning zero points took place at the ^{85}Rb working temperature to account for pressure shifts of the Rydberg energy levels.

Temperature stabilization and MW shielding

The measured optimal ^{85}Rb working temperature, $T = 42\ ^\circ$C, was ensured via hot air heating, as this method introduces little interference to MW fields propagating through the vapour cell. The air was heated and pumped through a specially designed hollow 3D-printed resin cell holder (Extended Data Fig. 1c), in which the heat exchange took place. The cell was enclosed in a MW-absorbing shield, made from a material with >30 dB loss at 14 GHz (LeaderTech EA-LF500) with sub-MW-wavelength apertures for optical beams; the shield also provided additional thermal isolation, reducing temperature fluctuations. The temperature of the shield inside, for the reference to blackbody radiation, was measured as 26–27 °C. The helical MW antenna was placed inside the shield and the collinear propagation was ensured with optical fields passing through an aperture at the backplate of the antenna (Extended Data Fig. 1f).

Frequency stabilization and calibration

The lasers in the experiment were stabilized (Extended Data Fig. 1a) to a narrowband frequency-doubled fibre laser (NKT Photonics, 1,560 nm), which was itself stabilized to a Rb cell via a modulation-transfer lock. The probe laser at 780 nm was stabilized to the frequency-doubled reference via an optical phase-locked loop. The 1,258 nm laser (decoupling), 960 nm laser (frequency-doubled to yield coupling light at 480 nm, Toptica DL-SHG pro) and 776 nm laser acting as LO were all stabilized to the reference at 1,560 nm using independent cavities via transfer locks. Laser fields were calibrated in low-intensity regimes with the use of EIT effects observed in the probe field transmission that registered on the control avalanche photodiode (Thorlabs APD120A, Extended Data Fig. 1f). The MW field, generated via an LMX2820 phase-locked loop frequency synthesizer, was coupled to the antenna and spectrum analyser (Agilent N9010A EXA) used for relative references of the field amplitude (Extended Data Fig. 1b). The absolute MW field amplitude was calibrated with a standard measurement of Autler–Townes splitting[46]. As a method of quantifying the converter's ability to distinguish photons from spectrally different sources, we performed a heterodyne measurement, yielding the converter's signal width $\Gamma_{sig} = 86 \times 2\pi$ kHz FWHM (Extended Data Fig. 1e). This value can be interpreted as a measure of the collective laser-locking phase noise.

Measurement techniques

Initially, the 776 nm signal was reflected from a bandpass filter and then passed through a series of free-space spectral filters (highpass, lowpass and 1.2 nm spectral width bandpass) and coupled to a fibre. Owing to the Gaussian characteristics of the beam (Extended Data Fig. 1d), coupling losses were negligible in this case (<25%). We applied

various detection methods as shown in Extended Data Fig. 1g. Additional filtering of the measurement of the noise-equivalent temperature was performed with an optical cavity (160 MHz spectral width, 80 finesse). The photon-counting measurements were performed with a single-photon detector (ID Quantique ID281 superconducting nanowire single-photon detector) with 85% quantum efficiency, <1 Hz dark count rate and 35 ns recovery time. As the detector's reliable response to incoming photons is on the order of $<10^7$ phot s^{-1}, calibrated neutral density filters were applied to the signal above this value. The autocorrelation measurement was performed on two channels of the single-photon detector after splitting the signal 50:50 with a fibre splitter. The heterodyne measurement was performed using a custom-made differential photodiode with the use of 776 nm LO laser, 20 mW power. The image of the beam profile (Extended Data Fig. 1d) was taken on a >50% quantum efficiency CMOS camera (Basler acA2500-14gm). The measurements of temperature (including those presented in Extended Data Fig. 1c) were performed with a calibrated thermal camera (Testo 883).

Data availability

Code availability

The codes used for the numerical simulation and the analysis of experimental data are available from the corresponding author upon request.

References

56. Krämer, S., Plankensteiner, D., Ostermann, L. & Ritsch, H. QuantumOptics.jl: a Julia framework for simulating open quantum systems. *Comp. Phys. Commun.* **227**, 109–116 (2018).
57. Marian, P. & Marian, T. A. Squeezed states with thermal noise. I. Photon-number statistics. *Phys. Rev. A* **47**, 4474–4486 (1993).
58. Borówka, S., Pylypenko, U., Mazelanik, M. & Parniak, M. Replication data for: continuous wideband microwave-to-optical converter based on room-temperature Rydberg atoms. *Harvard Dataverse* https://doi.org/10.7910/DVN/W7XZXB (2023).

Acknowledgements

Author contributions

S.B. and U.P. built the optical and MW set-ups. S.B. took the measurements and analysed the data, assisted by other authors. S.B., M.M. and M.P. prepared the figures and the manuscript. M.M. and M.P. developed the theory, assisted by S.B., who facilitated comparison with experiments. M.P. led the project, assisted by M.M.

Competing interests

The authors declare no competing interests.
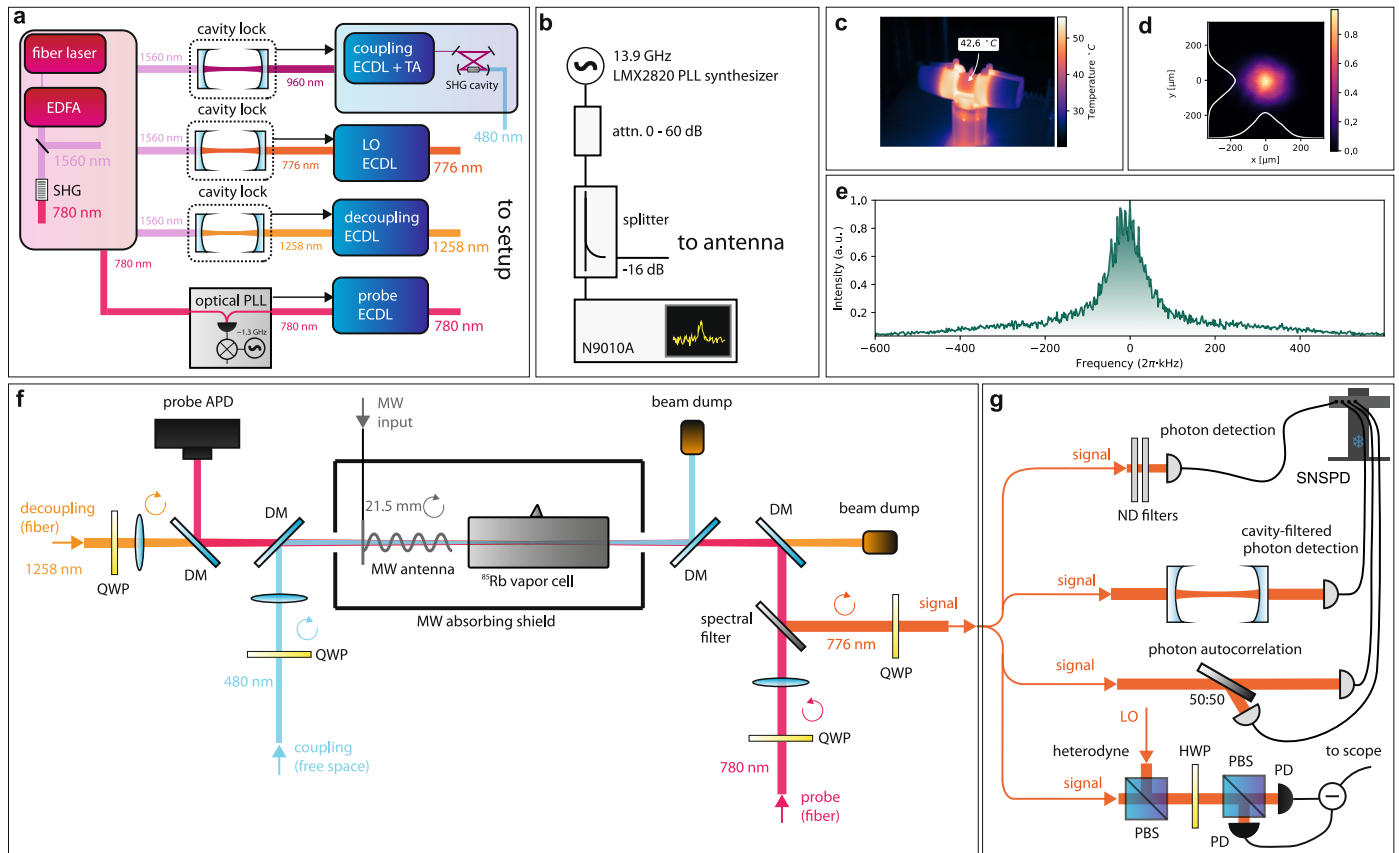
Additional information

Extended data is available for this paper at https://doi.org/10.1038/s41566-023-01295-w.

Extended Data Fig. 1 | Details of the entire experimental set-up. a, Laser system. A narrowband fiber laser at 1,560 nm serves as a frequency reference for the entire system. The laser is amplified via erbium-doped fiber amplifier (EDFA) and the frequency is doubled using a second-harmonic generation (SHG) process to 780 nm. The 960 nm external-cavity diode laser (ECDL) is amplified using a tapered amplifier (TA) and frequency-doubled via cavity-enhanced SHG to yield a coupling field at 480 nm. The 960 nm laser is stabilized to the master laser of 1,560 nm using a common cavity. A similar independent system is introduced for the stabilization of decoupling (1,258 nm) laser, likewise for local oscillator (LO) 776 nm laser. The second harmonic of the 1,560 nm fiber laser serves as a reference for offset-locking of the probe laser in an optical phase-locked loop (PLL). **b**, Microwave generation system. The generated microwaves are attenuated adequately and split into the spectrum analyzer for power and frequency references and to the antenna. **c**, Thermal image of the cell and cell holder. The constant temperature of the cell is assured with hot-air heating via hollow channels in the 3D-printed cell holder. **d**, The generated signal light exits the converter in a beam with a Gaussian profile shown in the image. **e**, Heterodyne measurement with LO yields spectrum of the converted signal: the residual

broadening of $\Gamma_{sig} = 86 \times 2\pi$ kHz FWHM is due to collective laser-locking phase noise. **f**, Scheme of the experimental setup: probe, coupling and decoupling laser beams are combined with dichroic mirrors (DM) into a collinear configuration, and focused inside a rubidium vapor cell of length 50 mm and diameter 25 mm with a MW helical antenna pointed there. The circular polarization of lasers is assured with quarter-wave plates (QWP). The probe (780 nm) signal is registered by an avalanche photodiode (APD), which enables laser calibration by observation of EIT features. Converted 776 nm signal is spectrally separated and coupled into a single-mode fiber. **g**, Different setups are used for detection, with single setup being used at a time. The detection setups include direct photon counting with optional attenuation, cavity-filtered photon counting, photon autocorrelation with two channels simultaneously, and heterodyne detection. For photon counting, a multichannel superconducting nanowire single-photon detector (SNSPD) is used. For heterodyne measurement we combine the signal with LO using a polarization beam splitter (PBS) and split the combined signal 50:50 with a half-wave plate (HWP) and a second PBS. The signal is then registered on a differential photodiode (PD).
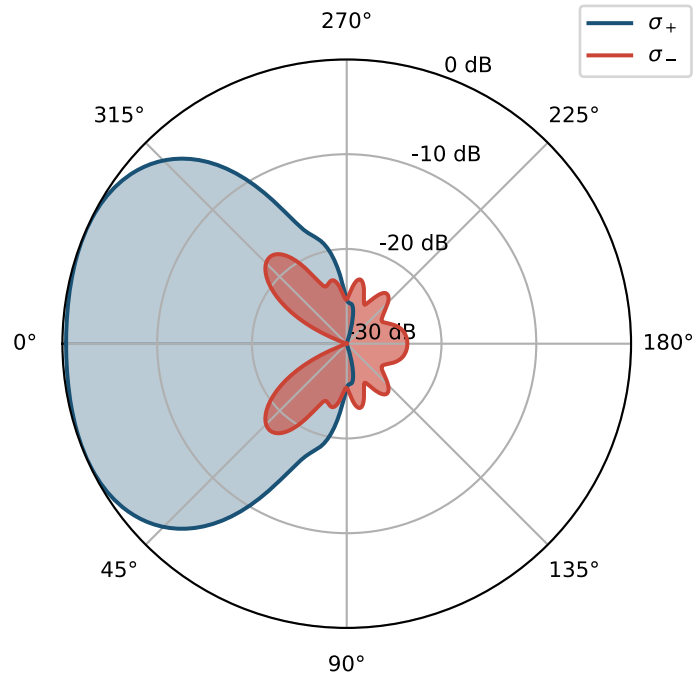
Extended Data Fig. 2 | Converter's spatial reception pattern. Calculated angular dependence of the MW conversion efficiency for two circular polarizations: σ_+ (antenna polarization) and orthogonal σ_-. The scale for both plots represents efficiency relative to the maximum of the σ_+ pattern in dB. The slight drop in efficiency at 0° is due to the Gouy phase of optical beams.